International Conference on Space Optics—ICSO 2022

Dubrovnik, Croatia

3–7 October 2022

Edited by Kyriaki Minoglou, Nikos Karafolas, and Bruno Cugny,

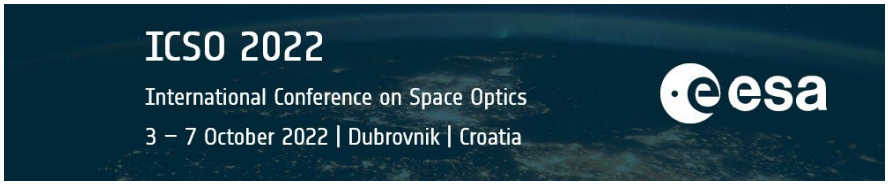

Solar Irradiance Sensor of RDM Exomars 2022 calibration

International Conference on Space Optics — ICSO 2022, edited by Kyriaki Minoglou, Nikos Karafolas, Bruno Cugny, Proc. of SPIE Vol. 12777, 1277774 · © 2023 ESA and CNES · 0277-786X · doi: 10.1117/12.2691378

Solar Irradiance Sensor of RDM Exomars 2022 calibration

J.J. Jimenez-Martín *[a], E. Garcia-Menendez [a], M. Gonzalez-Guerrer Bartolomé[b], J. Martinez-Oter[a], V. Apéstigue-Palacio[a], J. R. de Mingo [a], J. Rivas [a] , F. Serrano [a], S. Montalvo [a], A. García-Llases[b], I. Arruego[a]

[a] INTA – Instituto Nacional de Técnica Aeroespacial, INTA, Ajalvir Road 4.2 Km, Torrejón de Ardoz, 280850 Madrid, Spain.; [b] ISDEFE - Ingeniería de Sistemas para la Defensa de España S.A (as an external consultant at INTA), C/ Beatriz de Bobadilla, 3. 28040 Madrid, Spain.

ABSTRACT

This work presents the procedure and results of the optical calibration of the SIS'22 Solar_Irradiance_Sensor (SIS'22) of METEO, the meteorological stations for the Exomars 2022 Kazachok lander. The calibration procedure applied for this multichannel radiometer is an update of the ones carried out on the DREAM-SIS for the Schiaparelli [11]lander in ExoMars '16 and RDS (Radiation_and_Dust_Sensor) for the NASA/JPL Perseverance rover [7], both sensors designed and calibrated by INTA. The main innovation introduced since the DREAMS SIS is the inclusion of some corrections in the models to improve the uncertainties and improve the detectivity limit in low light conditions. Some of the changes introduced are also related to the new challenges that this instrument faced compared to the DREAMS SIS, which had an important impact on the calibration of the mean throughput and the angular dependence (ARF): Narrower FoVs, the necessity of a new characterization of the ARF and its "blocking zone", the use of UV channels, some channels were designed to measure diffuse light in spite of direct sun light, improvement of the offset characterization and a new spectral correction in order to reduce uncertainties.

Keywords: Solar Irradiance Sensor, Exomars, radiometer, calibration, Mars exploration.

1. INTRODUCTION

INTA Payloads and Space Science Department is involved in several scientific missions to Mars, developing solar irradiance sensors (SIS), name given for these devices which are multispectral multichannel radiometers for atmosphere studies.

Two SIS were manufactured before 2015: MetSIS (a radiometer intended to be launched onboard the for the Mars MetNet Precurssor Penetrator [1]) and the DREAMS-SIS for the ill-fated Shiaparelli lander of the ExoMars'16 mission [2] and [3]). [4], [5] contain a general description of DREAMS-SIS, as well as its objectives and operating principles that are common to all SIS.

Two more radiometers have been developed recently: the Radiation and Dust Sensor (RDS) for the next NASA/JPL Mars2020 Perseverance rover ([6], [7]) and the SIS'22 for the METEO meteorological stations of the Exomars 2022 Kazachok lander [8]. RDS is currently characterizing the atmospheric optical depth (AOD), estimating the scattering phase function of the Martian dust and detecting clouds and dust devils [9] and [10] on the surface of Mars, more concretely in the Jezero Crater.

This work is focused on describing the main updates that have been implemented in the procedure and analysis of the calibration of SIS'22 with respect to DREAM-SIS, and indicate the characteristics of the instrument that have been achieved in the hope that in the future it will reach the planet Mars

*jimenezmj@inta.es; phone (+34) 91 520 2093; http://www.inta.es

2. PRINCIPLE OF THE OPTICAL CALIBRATION

The method for the optical calibration of the SIS'22 is based on the calibration described on [11] and according to from [12] to [18]. This calibration model assumes that the light wavelength, the temperature, and the relative position of the radiative source can be considered as independent variables. Therefore, the output signal generated by each optical channel can be expressed as:

$$I(T,\varphi,\theta,E_{Sun}) = ARF(\theta,\varphi)\cdot TRF(T)\cdot R^{\lambda_2}_{\lambda_1\,Sun}\cdot E^{\lambda_2}_{\lambda_1\,Sun} + offset(T) \quad (1)$$

Where $E^{\lambda_2}_{\lambda_1}$ is the irradiance reaching the sensor between λ_1 and λ_2, which is the spectral band of the channel expressed in [W/m^2]; ARF is the Angular Response Function, that depends on the light incoming angle, (θ,φ) and it is dimensionless; TRF is the Thermal Response Function, that depends on the temperature (T) and it is dimensionless; and $R^{\lambda_2}_{\lambda_1\,Sun}$ is the 'mean throughput' (R) expressed in [A·m^2/W] that is defined like this:

$$R^{\lambda_2}_{\lambda_1}\left[A\cdot m^2/_W\right] = \frac{\int_0^\infty r(\lambda)\,E(\lambda)\,d\lambda}{\int_{\lambda_1}^{\lambda_2} E(\lambda)\,d\lambda} = \frac{\int_0^\infty r(\lambda)\,E(\lambda)\,d\lambda}{E^{\lambda_2}_{\lambda_1}} \quad (2)$$

Where r (λ) is the spectral throughput. Therefore, the $R^{\lambda_2}_{\lambda_1}$ of the channel depends on the optical system performance, because it depends on the spectral throughput (r (λ)), as well as on the light spectrum, through the spectral irradiance (E (λ)). Conclusively, the value of $R^{\lambda_2}_{\lambda_1}$ is associated to a particular light spectrum or a particular lamp or light source. It is not the same if the light source is a xenon lamp, halogen lamp or the light of the sun. For this reason, a sun simulator is used as the light source for the calibration. However, here is where an improvement has been introduced with respect to the previous instruments, and that is to introduce a correction due to the fact that the spectrum of the solar simulator is not in reality identical to the spectrum of the sun.

The reference conditions for the TRF and the ARF functions are defined to be, respectively, temperature of the unit under the responsivity calibration, and a perpendicular incidence of the light on every channel's sensor. In other words, TRF is 1 at this temperature and ARF is 1 when light reaches the photodiodes perpendicularly (normal incidence).

The instrument provides a number of 'counts' proportional to the photocurrent of photodiodes:

$$\underbrace{S_{SIS}(counts)}_{Instrumetn\ Digital\ Signal} = \underbrace{K\left(Counts/_A\right)}_{Constant\ that\ depend\ on\ the\ electronic} \cdot \underbrace{I(A)}_{\substack{Photocurrent\\ or\ even\\ temperature}} \quad (3)$$

So, it is possible to work directly in 'counts' in the equation (1).

Four independent characterizations are needed in order to calibrate the SIS'20 and to get the four parameters of (1): the angular dependence (ARF), the thermal dependence (TRF), the offset in dark conditions and the mean throughput under the sun light (RSun) of the channel being calibrated:

- **Offset calibration**: In dark conditions the temperature is swept to cover the entire thermal range.
- **Optical Thermal calibration (TRF – Thermal Response Function)**: the optical power and the angle of incidence of the light on every sensor's surface are fixed and only the temperature is made to change in order to evaluate the TRF.
- **Angular calibration (ARF – Angular Response Function)**: the optical power and the temperature are fixed and only the light incidence angle on every sensor's surface is made to change in order to evaluate the ARF.
- **Mean throughput measurement**: the optical power lamp is excited in four steps, increasing irradiance from a low level to a high one at room temperature with the light at normal incidence over each optical channel. Experimental data acquired are fitted to a linear curve where the slope is the mean throughput (RSun).

3. OPTICAL CHANNELS SIS'22 DESCRIPTION

SIS'22 has different optical channels composed of silicon photodiodes plus interference filters and Field of View Masks (FoV-Mask). These configurations allow them to work with different wavelength ranges (spectral bands) to target different parts of the sky. SIS'22 hosts twelve detectors in its six lateral faces (with an elevation of 20 degrees) and five in the top surface (pointing to the zenith). The Figure 1 shows a schematic of the SIS and how its channels are distributed in the azimuthal and zenithal angles, fixing also the reference system used in all the analyses.

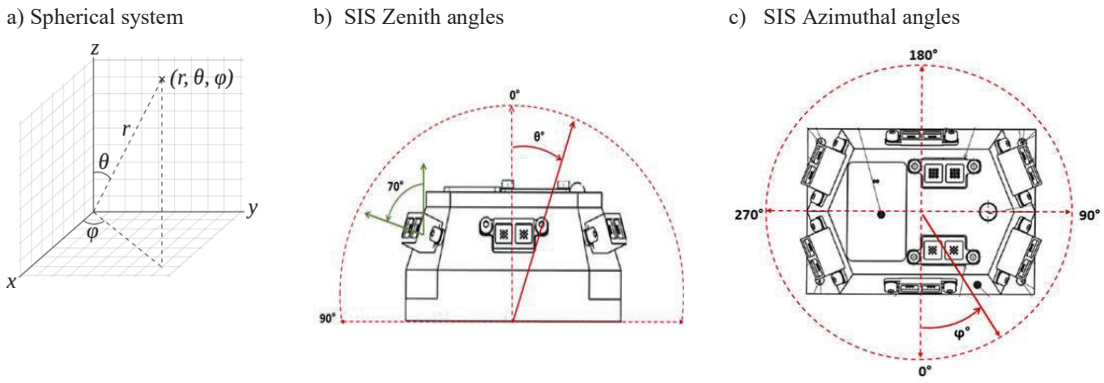

Figure 1. (a) Spherical coordinates reference system ; (b) SIS zenith angle [θ]; (c) SIS azimuthal angle [ϕ].

According the reference system of the SIS showed in Figure 1 characteristic of each lateral and top optical channels are collected in Table 1

Table 1. Optical channels characteristics and angle coordinates.

SIS CHANNEL PROPERTIES						
REF	SIDE	Name	Wavelength (nm)	FoV (°)	AZIMUTH (***φ***°)	ZENITH ANGLE (***θ***°)
#1	TOP	Total Sky	190 - 1200 nm	± 90	Not. Apply	0
#2	TOP	IR	750 ± 5 nm	± 40	N. A.	0
#3	TOP	UV	250 - 400 nm	± 40	N. A.	0
#4	TOP	O_3-255	255 ± 5 nm	± 15	N. A.	0
#5	TOP	O_3-295	295 ± 5 nm	± 15	N. A.	0
#1	SIDE	IR	750 ± 5 nm	± 5.5	0	70
#2	SIDE	UV	250 - 400 nm	± 5.5	0	70
#3	SIDE	IR	750 ± 5 nm	± 5.5	66	70
#4	SIDE	UV	250 - 400 nm	± 5.5	66	70
#5	SIDE	IR	750 ± 5 nm	± 5.5	111	70
#6	SIDE	UV	250 - 400 nm	± 5.5	111	70
#7	SIDE	IR	750 ± 5 nm	± 5.5	180	70
#8	SIDE	UV	250 - 400 nm	± 5.5	180	70
#9	SIDE	UV	250 - 400 nm	± 5.5	246	70
#10	SIDE	IR	750 ± 5 nm	± 5.5	246	70
#11	SIDE	UV	250 - 400 nm	± 5.5	292	70
#12	SIDE	IR	750 ± 5 nm	± 5.5	292	70

4. SIS CALIBRATION

4.1 Offset

The thermal calibration was carried out in the LT/HT thermal chamber of the SPASOLAB facilities, at INTA (building A-06), in Torrejón de Ardoz, Madrid (Spain). It was performed in darkness conditions **on the 29th of November of 2018.**

The RDM SIS'20 FM unit was fixed to a horizontal interface and then to the base plate with proper screws. The temperature was varied between 50ºC and -145ºC approximately, in several steps. A thermal bake-out at +50 ºC was done before starting the test. To ensure the cleanliness and dryness of the chamber and to guarantee that the N_2 gas penetrates in the SIS and its optical parts, vacuum up to ~5 mbar was done. After that, the chamber was filled up with N_2 gas again. The chamber was vacuumed up and filled up 3 times in order to assure that the instrument and the chamber were completely dry and clean of impurities.

Three thermocouples were used to monitor the temperature of the unit. And check not to exceed the temperature requirement, especially due to the presence of a mini-spectrometer that has lower range of working temperature that it is placed inside.

In order to configure the system for this measurement the SIS is placed, horizontally, on the LT/HT thermal chamber with a 50 cm diameter quartz window (Figure 2). The chamber is closed and the quartz windows is covered to ensure darkness during measurements.

The calibration EGSE is configured to perform a measurement of every channel several times per minute (about 16 times/minute).

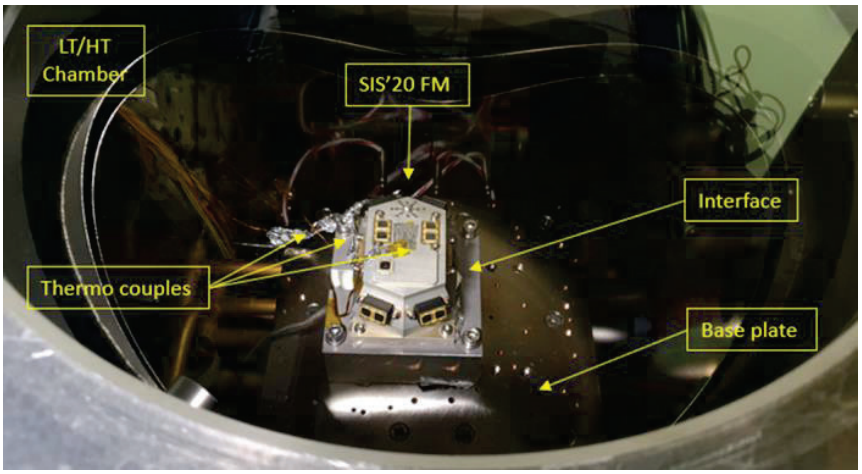

Figure 2. Optical channels distribution of RDM SIS'20.

In this configuration, the temperature is scanned firstly from 50ºC to -145ºC, and back from -145ºC to 50ºC. Step by step, the temperature describes a ramp-up and then a ramp-down with a thermal rate fixed in 2ºC/min.

In order to know the relation between the value of the temperature in Celsius degrees and the value in 'counts' given by the channels output, a thermal characterization has been performed, obtaining the following:

$$\mathrm{T}\ (^{\circ}\mathrm{C}) = 0.005964 \cdot \mathrm{Temperature}\ (\mathrm{'counts'}) - 291.51 \tag{4}$$

New offset correction

The experimental data from every channel have been fitted to the same equation explained in [11] plus a corrections:

$$\mathrm{Offset\ (Cpunts)} = \underbrace{p1 \cdot e^{\left(\frac{-T}{p2}\right)}}_{Dark\ current} + \underbrace{p3 + p4 \cdot T}_{'Electronic'\,offset} + f(T) \tag{5}$$

Where $f(T)$ is the **new correction term** and it is different for low temperatures than for high temperatures.

$$f_{low\_T}(counts) = A0 + A1 \cdot T + A2 \cdot T^2 + A3 \cdot T^3 + A4 \cdot T^4 \quad (6)$$

$$f_{high\_T}(counts) = y0 + \left[4 \cdot A \cdot e^{\left(-(T-xc)/w\right)}\right] \Big/ \left[1 + e^{\left(-(T-xc)/w\right)}\right]^2 \quad (7)$$

Offset results

Figure 3 to Figure 6 show the experimental data and the fittings made as well as the residual of the fitting which is the difference between the experimental points and the mathematical fit. It can be seen how the residuals are normally less than 10 counts and only for some channels do they exceed 20 at very high temperatures. Without applying the new correction, the residuals reached values of 300 counts at very high temperatures and although it was not expected that the instrument would reach these conditions, it was preferred to include it. The IR lateral channel, not shown in the graph, have similar behavior.

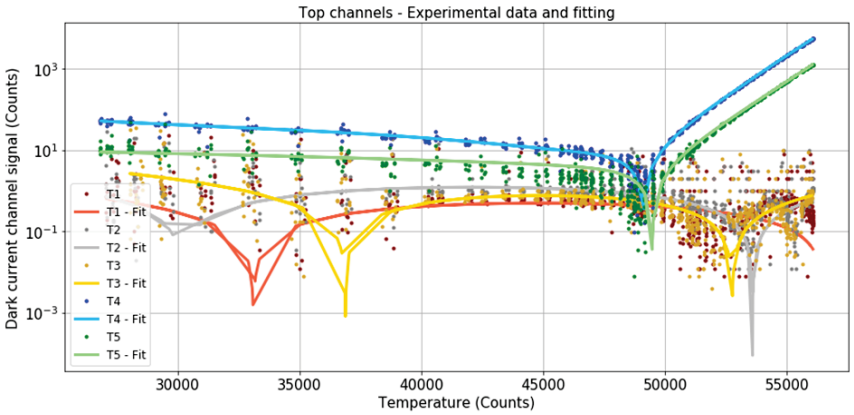

Figure 3. TOP channels dark signal absolute value data and fitting in a logarithmic scale.

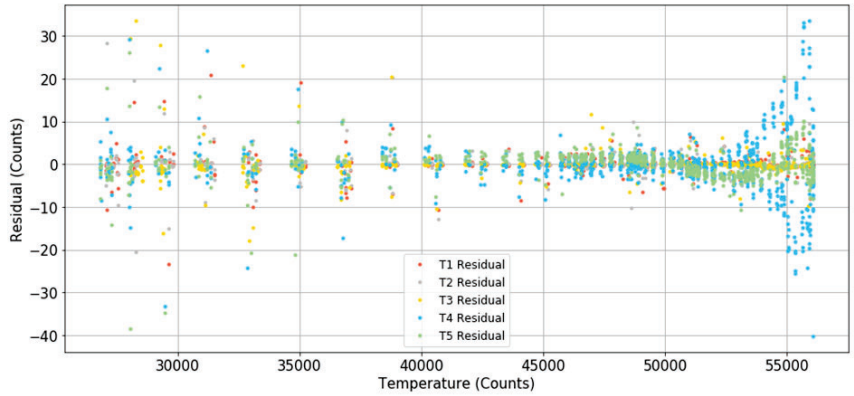

Figure 4. Difference between the experimental value and the mathematical fitting performed for TOP channels

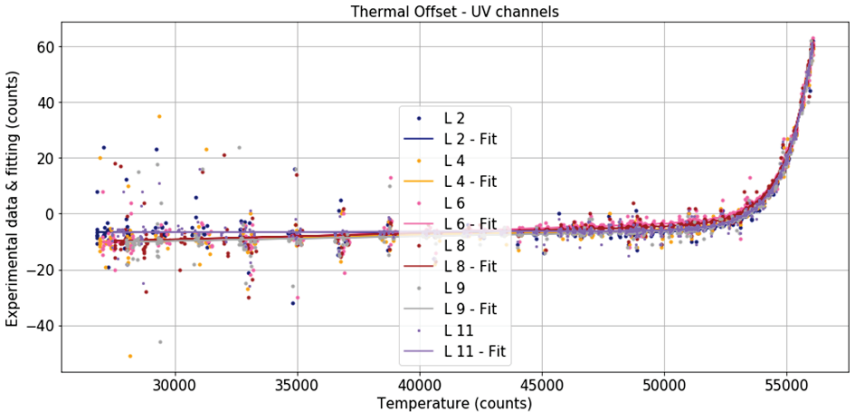

Figure 5. LATERAL UV channels dark signal absolute value data and fitting in a logarithmic scale.

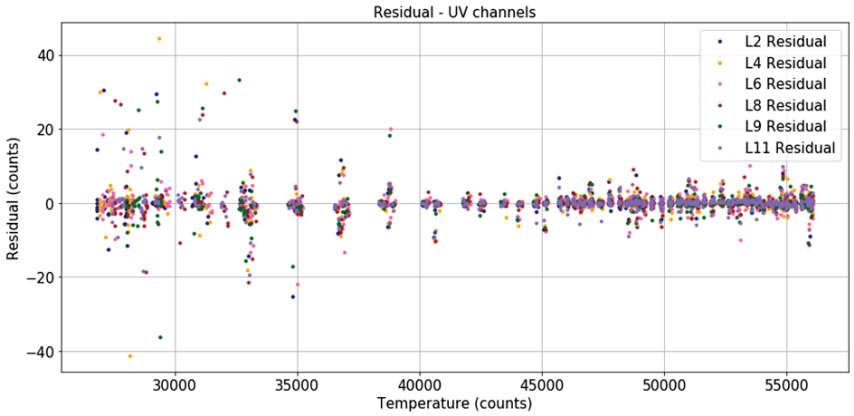

Figure 6. Difference between the experimental value and the mathematical fitting performed for LATERAL UV channels

Once in Space, there are some factors that can change the relationship between the temperature and the offset signal, as for example, the ionizing and non-ionizing radiation over the photodiodes and over the electronics. This effect does not represent a real problem if the offset keeps in low enough values. In any case, the instrument provides information on this degradation by the measurements of the dark current channel, which is always done in dark conditions.

Moreover, at the beginning of the night there is not enough light signal and the temperature will start to decrease and some offset verification will be done at different temperatures over every channel. These data are to be be used as offset checking.

4.2 Thermal Response Function – TRF

The TRF is the normalized photocurrent signal versus the temperature, that is, a factor that modifies the responsivity of every channel depending on the temperature. TRF includes all factors that have an effect on the responsivity of the optical channels: changes in the transmittance of the optical parts, changes in the responsivity of the photodiodes and thermal drifts in the electronics of the unit.

The optical thermal response (TRF) calibration was carried out in the LT/HT thermal chamber of the SPASOLAB facilities on **the 26th, 29th and 30th of November of 2018** under constant illumination.

The photocurrent of the optical channels is intended to be measured simultaneously with the temperature by using different internal sensors. During the test, three extra thermocouples are used to monitor and control the temperature of the LT/HT chamber, the unit and the interface. Figure 7 shows the set-up for this thermal calibration test.

The photocurrent values have been normalized to the mean work temperature of the range (approximately 20 ºC = 52000 "counts") and their dependency with the temperature has been fitted to the equation (8)

As it was done in the previous thermal offset calibration, the temperature is scanned firstly from 50º to -145º C, and back from -145º C to 50º C. Step by step, the temperature describes a ramp-up and then a ramp-down. The thermal rate was fixed in 2º C/min.

A solar sun simulator is used to illuminate the optical sensor at a constant level of irradiance during the thermal calibration test. It has to be configured not to saturate the generated photo signal at low temperature by using an extra optical filter with a transmittance of 50% + 35%.

The RDM SIS'20 FM unit is commanded to measure under low and high gain and each signal is represented versus their own temperature channel.

Once the results of the measurements are normalized, the data from every channel have been fitted to the next equation:

$$\boldsymbol{TRF(T)} = \boldsymbol{P_5} + \boldsymbol{P_6}(\mathrm{T(Counts)} - \mathrm{Tref}) + \boldsymbol{P_7}(\mathrm{T(Counts)} - \mathrm{Tref})^{\boldsymbol{2}} \quad (8)$$

Where T is the RAW temperature sensor signal, chosen for each evaluated channel of the SIS expressed in 'counts'. In this analysis, the chosen value of the temperature of reference was 51980 counts (Tref), which has been obtained evaluating the mean work temperature of different test carried out in the thermal calibration under low gain configuration.Figure 8 and Figure 9 show the experimental data, statistical fits and residual of the TOP channels. The lateral channels have similar behavior.

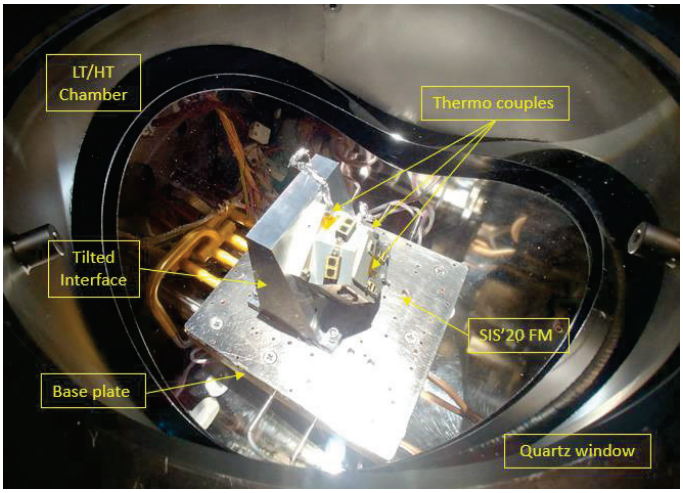

Figure 7 Set-up for tTRF Calibration with the SIS'20 FM installed on the tilted interface to evaluate the TRF of two lateral channels.

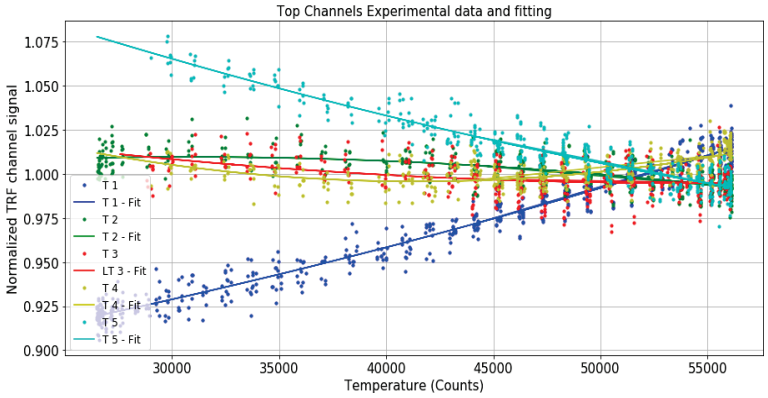

Figure 8. TOP channels TRF signal value data and fitting.

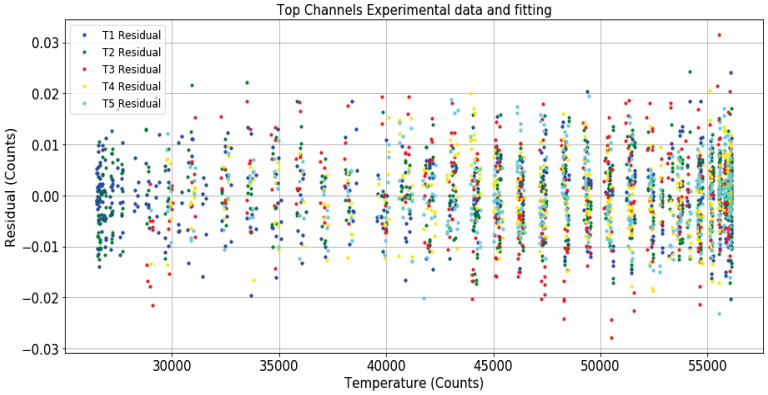

Figure 9. Difference between the experimental value and the mathematical TRF fitting performed for TOP channels

4.3 ARF

The ARF calibration provide us the Angular Response Function (ARF), this function depends on the light incoming angle and takes values between 0 and 1.

This function will give us information about the angular response of the optical channels by measuring the photocurrent of each channel when the irradiance and the temperature are fixed and only the light incidence angle is changing for the zenith and azimuthal coordinates by using a high precision rotating setup [11]. The angular dependence calibration test has been done in INTA facilities on **13th and 14th of July of 2018.**

The lamp used in this test had to be replaced by one with more UV light. This new lamp has, however, has less overall intensity, and the data obtained have been noisier.

The source of light chosen was a xenon/mercury lamp and it is placed approximately at a distance of 4.5 m from the system where the unit is located. This distance will reduce the emission mismatches and allow us to consider the light that reaches the instrument is uniform and has a flat wave front. The lamp was turned on at least 30 minutes before starting de test to avoid spectral changes in the emission and to keep the light under constant emission during the test. The ambient light is turned off before starting the test. The SIS unit was set in the two-axis rotator.

Once we have it well aligned with the central part of the top, pointing normally to the light source, the azimuth and zenith angles from the rotator are reset to (0°, 0°) as the new origin of coordinates. Then, the test is started by making a very detailed angular sweeps for each channel from $\vartheta = [0°, 110°]$ and $\phi = [0°, 360°]$. Figure 10 shows the map of every pair of points considered in the calibration analysis programmed and controlled with a SW specially developed for this task.

The offset and TRF corrections should be applied on the RAW data before this analysis. We have also to use the SIS reference system (θ, φ), as it was shown in Figure 1.

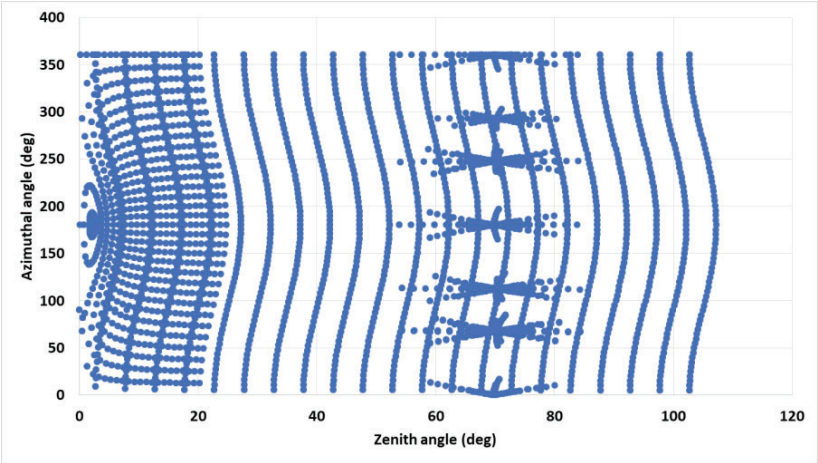

Figure 10. Pairs of (ϑ,ϕ) coordinates including the lateral and top sweeping calibration procedure. Y axis shows values of zenith angle whereas x axis shows azimuthal angles between -150° and 200°.

These corrected experimental data obtained during the test are normalized to the ones in the center of each face using (9) as the maximum value and, on the other hand, considering the minimum value the ones located at the end of the experimental data 'blocking area' between [90°, 100°] zenith angles from the RDS reference system.

$$ARF\ (\vartheta, \varphi) = \frac{(I\ (\theta, \varphi) - I_{\vartheta=90}^{\vartheta=100}}{I(\theta_{\perp}, \varphi_{\perp})} = \frac{I\ (\theta, \varphi) - I_{min}}{I_{max}} \tag{9}$$

Where Imax is the current measured when a face under study points directly to the light source.

The process of running the test and the analysis up to this point is similar to that described in [11], but the analysis explained below is entirely new.

New ARF analysis

The experimental data have been fitted according to (10) composed by three functions; and "I min" is the signal when the light is reaching the channel with an angle higher than 90 DEG and it is supposed that the photons cannot hit the detector.

The experimental data already processed have been fitted by using the next equation that is composed of three functions:

$$ARF(\alpha) = \underbrace{z_0 + C \cdot \widetilde{F_1(\alpha)}}_{\text{Based on the FoV mask geometry}} + \underbrace{F_2(\alpha) + F_3(\alpha)}_{\text{Corrections to adjust the reflectivity of the walls (the "tails") and the "blocking zone"}} \tag{10}$$

Where 'α' is the angle formed between the light incident direction and the direction where the FoV of the channel under the study is pointing at; 'z0' is the offset signal.

The angle 'α' referring to the SIS reference system can be expressed like:

$$\cos\alpha\ (\theta, \varphi) = \left| \left[\sin(x_\theta) \sin(\theta) \left[\cos(y_\varphi) \cos(\varphi) + \sin(y_\varphi) \cdot \sin(\varphi) \right] + \cos(x_\theta) \cdot \cos(\theta) \right] \times \sqrt{(aux_\theta)^2 + (aux_\varphi)^2} \right| \tag{11}$$

Where:

- θ and φ are the zenith and azimuthal angles of the light incident direction respectively.

- aux_θ and aux_φ are two auxiliar variables based on the internal azimuthal angle between the light incidence angle and the pointing direction of each channel. It also allows to the FoV not being totally symmetric but some elliptical shape on their FoV values. The corresponding equations are:

$$\begin{aligned} aux_\theta &= W_\theta * \cos(rho + rotation) \\ aux_\varphi &= W_\varphi * sin(rho + rotation) \end{aligned} \tag{12}$$

- W_θ and W_φ are the widths of the fitted function in each direction. These parameters allow to break the revolution symmetry. So that, if W_θ is equal to W_φ, then the FoV mask has a perfect response with a revolution symmetry, in other case has a "elliptical response".
- rho is the projection of the cross product between the internal angle existing between the incident light (θ, φ) and the fitting coordinates of each optical channel (x_θ, y_φ).
- $(x_\theta \cdot W_\theta)$ and $(y_\varphi \cdot W_\varphi)$ are the zenith and azimuthal angles of the direction where the FoV mask is pointing at, obtained in the fitting.
- $rotation$ is the inclination of the FoV obtained in the corresponding fitting.

F1(α) corresponds to an analytic function based on the geometry of the FoV Mask. It is a function that depends on radius (r) and length (l) of the cylinders in de FoV mask, as can be seen in (13).

This equation is not defined out of the FoV limits.

$$F_1(\alpha) = \left[2r^2 atan\left[\frac{\sqrt{4r^2 - l^2 tan^2\alpha}}{l\tan\alpha}\right] - \frac{l\tan\alpha\sqrt{4r^2 - l^2 tan^2\alpha}}{2}\right] \tag{13}$$

Where 'r' and 'l' have specific values depending on the FoV of the evaluated channel: Lateral channels (± 5 DEG): r = 0.25 mm, l = 5.2 mm; Top 2 and Top 3 channels (± 40 DEG): r = 0.5 mm, l = 1.2 mm; Top 4 and Top 5 channels (± 15 DEG): r = 0.25 mm, l = 1.86 mm.

On the other hand, F2(α) is a correction to adjust the internal reflectivity of the cylinder walls, it is not based in any physical model but on experimental data. More than 10 expressions have been tested in order to find F2. It basically helps to accurately model the 'tails' of the ARF function especially close to the limit of the FoV.

This function is written as follows:

$$F_2(\alpha) = A \cdot \exp[-exp(-(\alpha - xc)/\omega) - ((\alpha - xc)/\omega) + 1] \tag{14}$$

Where Xc is the distance between the maximum value of F2 and the maximum value of F1, ω modulates the width of this function. A is the amplitude of this function.

Finally, function F3(α) is another correction to adjust the effect of the 'blocking zone' out of the range of the FoV to fit properly this angular dependence (15) including stray light effects. This equation has the same shape as F2 but it acts in a lower level as it could be seen in the next sections.

$$F_3(\alpha) = AA \cdot \exp[-exp(-(\alpha - xxcc)/\omega\omega) - ((\alpha - xxcc)/\omega\omega) + 1] \tag{15}$$

The selection of F1 (14) and F3 (15) is based on the goodness of the fitting, the residual obtained after the fitting and its simplicity and lower numbers of parameters. Another important point in the selection of this ARF function has been that in spite of not being a physical model, the parameters do have a real meaning that can be interpreted (Amplitude, position of the maximum, width…).

Having all these ideas into account, the correct way to use this equation, after normalizing the data before the analysis, is to force the condition ARF = 1 in all the scenarios when light is reaching perpendicularly the photodetectors (α = 0). This condition can be achieved by dividing the amplitude parameters as 'C', 'A' and 'AA' by the maximum value of ARF in the pointing direction, to obtain the final results.

ARF results

The Figure 11 shows an example of the F1, F2, F3 and ARF contributions in the case of a top channel (+/- 15 DEG of FoV). The Figure 12 are three graphs, the first one shows the experimental points of TOP 3 and (blue dots) and the data proportional to the fit (orange dots); the middle graph shows the residual (the difference between the experimental data and the fit); and the graph below shows the residual expressed as a percentage of the ARF value. Values above 10% would exceed the project requirements. This is a typical wide FoV channel compartment.

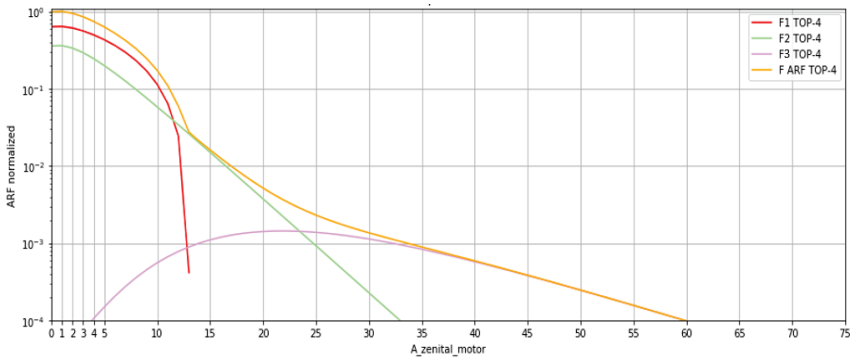

Figure 11: ARF, F1, F2 and F3 in a general case of a top channel.

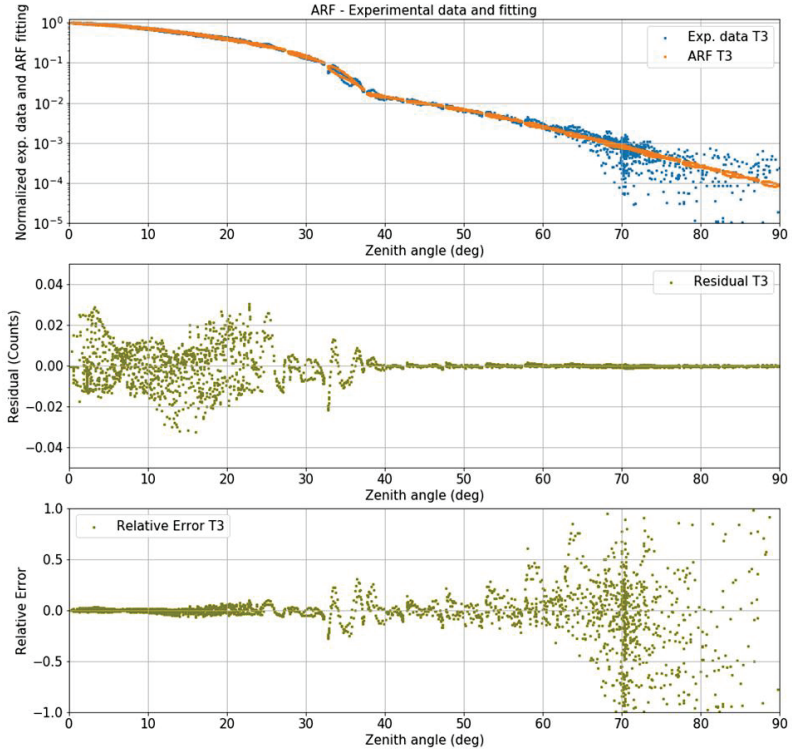

Figure 12: Angular Response Function – ARF of the TOP-3 channel (FoV = ± 40°) (orange), experimental data measured (blue dots) versus the corresponding zenith angle of the instrument reference system [top graph]; Residual from the ARF fitting [middle graph]; and relative error from the analysis [bottom graph].

Figure 13 shows three lines, two read on the left axis which are the ARF value (black line) and the confidence interval (dashed red line) and another one read on the right axis which is the uncertainty expressed as a percentage (blue line). It can be seen that up to an angle of 60 the uncertainty is less than 1% and up to an angle of 80 it is 10%.

Figure 14 shows the ARFs, confidence intervals and percentage uncertainties for all TOP and lateral channels.

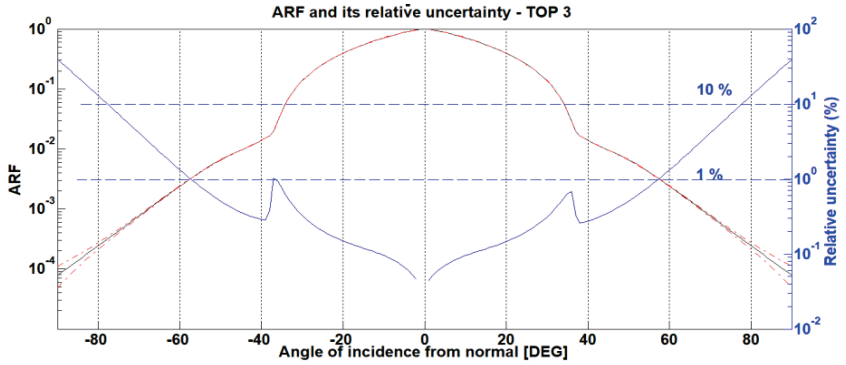

Figure 13. Top 3 ARF and its uncertainty analysis. ARF value (black line) and the confidence interval (dashed red line) read on the left axis and the uncertainty expressed as a percentage (blue line) read on the right axis.

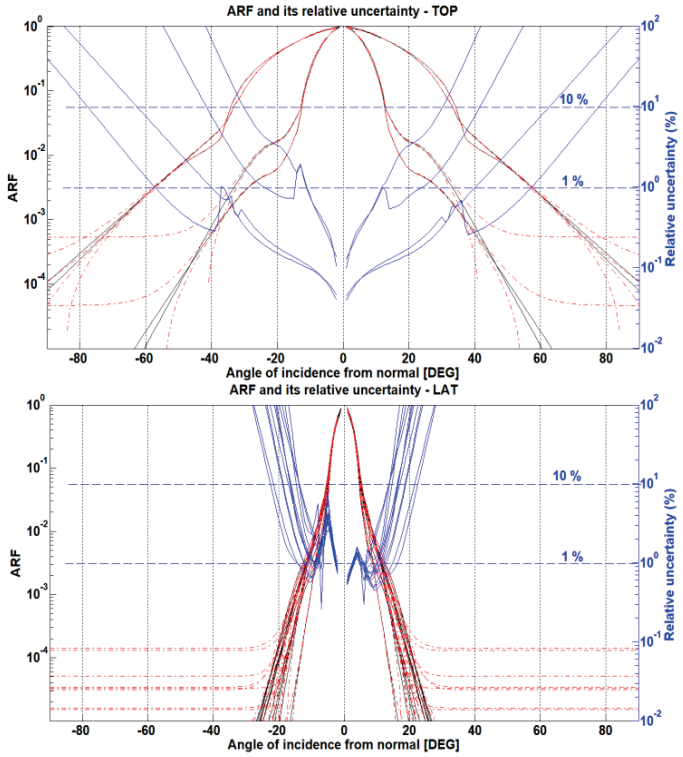

Figure 14. TOP and Lateral channels ARF and its uncertainty analysis. ARF value (black line) and the confidence interval (dashed red line) read on the left axis and the uncertainty expressed as a percentage (blue line) read on the right axis.

4.4 Responsivity

The unit was mounted in the 2-axis rotator parallel to the optical work plane under the simulator beam. The solar sun simulator should be turned on with an irradiance levelthat does not saturate the photo signal of the optical sensors. Reference measurements are taking before each test at all the different levels of irradiance used in the calibration with a spectroradiometer in order to correct the value of irradiance that reach each photo diode depending on their wavelength working range.

Once SIS unit is set and aligned under the beam light, the azimuth and zenith angles from the rotator are reset to (0°, 0°) as the origin of coordinates. Then, every lateral and top photodiodes will be characterized by varying the azimuthal and zenith coordinates (ϑ, ϕ) in order to obtain the signal under normal incidence of light for each one. Then, it is possible to obtain different irradiance levels, which can be achieved by using different optical filters and sun simulator configurations.

A total of 13 illumination levels have been used, although not all of them are suitable for all channels, as some of them saturate at the higher light levels and others give a signal that is too low and close to the noise level at the lowest. Three levels of power supply current have been combined in the simulator (93 A, 83 A and 73 A) and up to four different neutral filters (50%, 35%, OD1.2 and OD3) have been used.

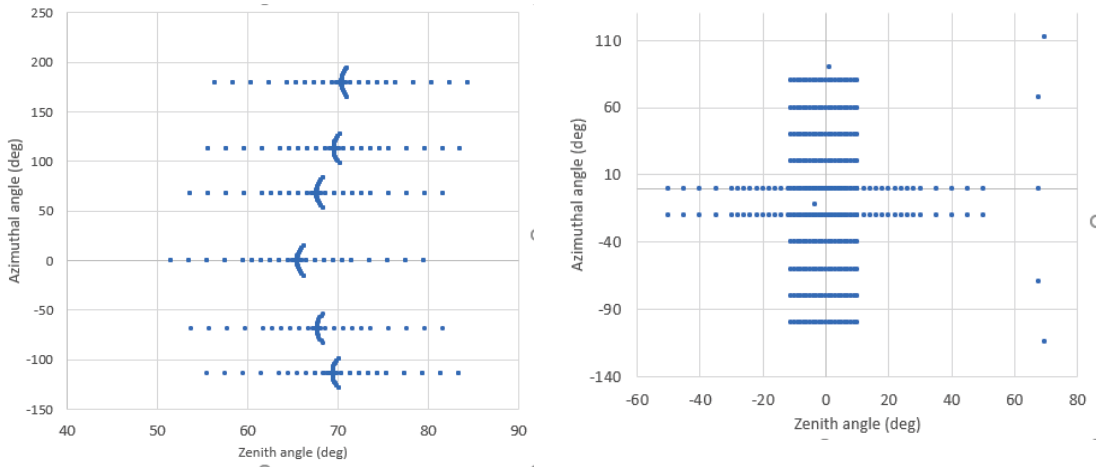

Figure 15: Matrix of points for the lateral channels (left). Matrix of points for top channels (right).

Spectral Correction

As seen in equation (2) the average responsivity depends on the shape of the incident light spectrum. For this reason, if the light used during calibration is not the same as the light spectrum of the Sun (AM0), the data obtained will not be valid. A solar simulator was used with a spectrum that is quite similar to that of the Sun, but it is not identical, so the improvement that has been introduced is to calculate a correction for this effect. For this calculation, the theoretical spectral responsivity given by the manufacturer of the components has been used to calculate the average responsivity under the solar simulator illumination:

$$R_{Sun\_simulatr}{}_{\lambda_1}^{\lambda_2}\left[A \cdot m^2/W\right] = \frac{\int_0^{\infty} r(\lambda)\, E_{Sun\_simulator}(\lambda)\, d\lambda}{\int_{\lambda_1}^{\lambda_2} E_{Sun\_simulator}(\lambda)(\lambda)\, d\lambda} \tag{16}$$

And also to calculate what would be the average responsivity with an ideal solar spectrum:

$$R_{AM0}{}_{\lambda_1}^{\lambda_2}\left[A \cdot m^2/W\right] = \frac{\int_0^{\infty} r(\lambda)\, E_{Sun\_simulator}(\lambda)\, d\lambda}{\int_{\lambda_1}^{\lambda_2} E_{AM0}(\lambda)(\lambda)\, d\lambda} \tag{17}$$

The correction factor is the quotient between the two:

$$Spectral\ Correction\ Factor = \frac{R_{Sun\_simulatr}{}_{\lambda_1}^{\lambda_2}}{R_{AM0}{}_{\lambda_1}^{\lambda_2}} \quad (18)$$

Table 2. Spectral Correction Factors to each specific channel

Channels → EP2	Neutral filter	TOP 1 [190 - 1200 nm]	TOP 2 (750 ± 5 nm)	TOP 3 (250 - 400 nm)	TOP 4 (255 ± 5 nm)	TOP 5 (295 ± 5 nm)	LATs UV (250 - 400 nm)	LATs IR (750 ± 5 nm)
	50 %	1.03529	1.00002	1.00208	1.00421	1.00207	0.99998	1.00211
@93	50% + 35%	1.02030	1.00003	1.00189	1.00180	1.00168	1.00002	1.00189
[A]	50% + O.D 1.2	-	1.00010	1.04256	1.18775	1.00485	1.00010	1.04256
	50% + O.D 3	-	1.00279	0.72407	1.00749	0.86658	1.00279	0.72407
	50 %	1.04293	1.00004	0.99866	1.00129	1.00248	1.00000	0.99868
@83	50% + 35%	1.02712	1.00006	0.99866	1.00121	1.00258	1.00001	0.99868
[A]	50% + O.D 1.2	-	1.00013	1.05715	1.00853	1.01660	1.00013	1.05715
	50% + O.D 3	-	0.99465	1.28827	1.02444	0.95784	0.99465	1.28827
	50 %	1.04342	1.00005	0.99705	1.00364	1.00287	1.00000	0.99707
	50% + 35%	1.02472	1.00003	0.99651	0.99954	1.00325	0.99997	0.99652
@73	35%	1.02580	1.00009	0.99790	1.00160	1.00309	1.00004	0.99792
[A]	50% + O.D 1.2	-	1.00011	1.04451	1.04743	1.01022	1.00011	1.04451
	50% + O.D 3	-	1.00014	1.02070	1.01903	1.00200	1.00014	1.02070

Responsivity results

The experimental data acquired are fitted to a single straight line, where the slope is the responsivity (Figure 16 and *Figure 17*). uncertainties in the measurements need to be considered:.

- Signal's amplitude, obtained throughthe offset analysis, is around 5 *counts* for each optical channel; and we have the uncertainty in the irradiance measured by the spectro-radiometer and the working plane non-uniformity (Table 3).

Table 3 Uncertainties given by the spectroradiometer for every type of photodiode

σ	K	TOP 1 [190 - 1200 nm]	TOP 2 (750 ± 5 nm)	TOP 3 (250 - 400 nm)	TOP 4 (255 ± 5 nm)	TOP 5 (295 ± 5 nm)	LATs IR (750 ± 5 nm)	LATs UV (250 - 400 nm)
66 %	1	2.82 %	2.25 %	3.32%	6.0 %	2.75 %	2.25 %	3.32 %
95.45 %	2	5.63 %	4.5 %	6.65 %	12 %	5.5 %	4.5 %	6.65 %

The responsivity reaches higher values for IR lateral channels than for the UV lateral and the top ones. The uncertainty of the measurements is ruled by the spectroradiometer uncertainty. It can be seen in the Figure 18 that show the fitting slope and its error bars. This slope is the responsivity in low gain.

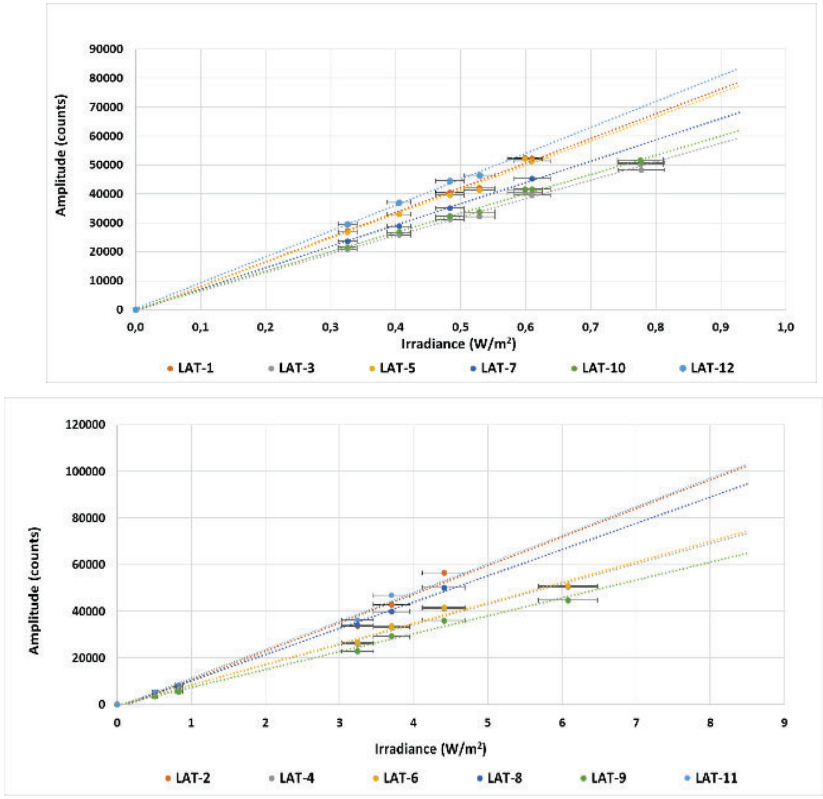

Figure 16. Experimental amplitude signal data from UV Lateral and IR channels for EP2 sun simulator under variable irradiance obtained by using 50% and 35% filters configuration.

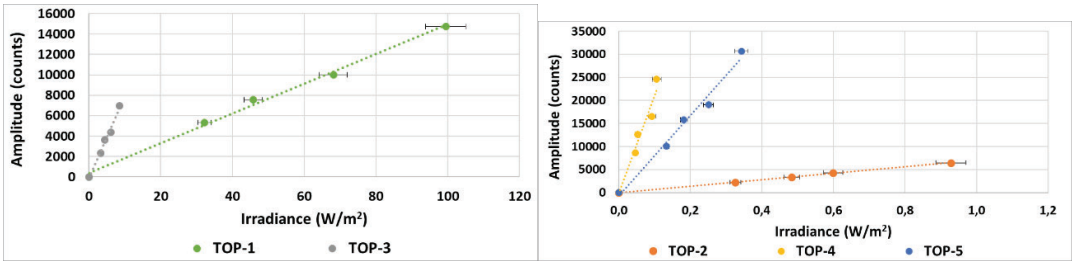

Figure 17. Experimental amplitude signal data from Top channels for EP2 sun simulator under variable irradiance obtained by using 50% and 35% filters configurations.

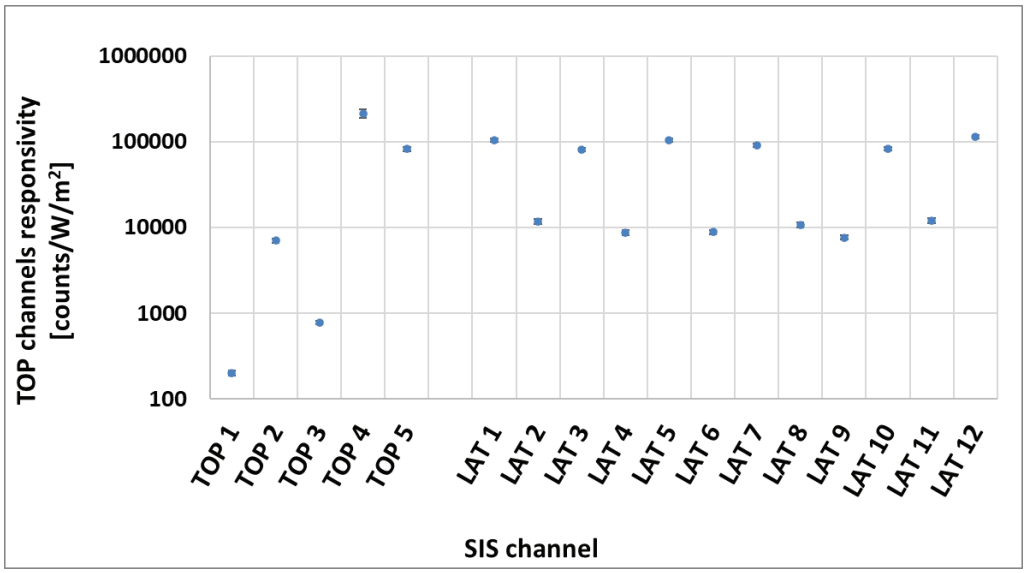

Figure 18. SIS optical channels responsivity and their uncertainties in logarithmic scale.

The gain factor for the high gain is the ratio between the value in high and low gain and under the same irradiance level, temperature value and incident angle.

$$\text{Gain factor} = \frac{\text{Signal in HIGH gain configuration}}{\text{Signal in LOW gain configuration}}$$

Eq. 1

Excluding the saturated channels and comparing the valid ones with the results of the same configuration in low gain, as a function depending on a common azimuthal angle. Finally, the average of all these data will result in the Gain Factor value for each channel independently.

To obtain this factor, two different files of the responsivity calibration test have been treated and analyzed. The result of each gain factor obtained in this analysis is show in Table 4 showing the values for every TOP and LATERAL channel, and the corresponding standard deviations.

Table 4. Gain factor

	TOP 1	*TOP 2*	*TOP 3*	*TOP 4*	*TOP 5*
Gain Factor	38.23	38.04	38.10	38.43	38.07
Std. deviation	0.98	0.53	0.63	0.43	0.44

	LAT 1	*LAT 2*	*LAT 3*	*LAT 4*	*LAT 5*	*LAT 6*	*LAT 7*	*LAT 8*	*LAT 9*	*LAT 10*	*LAT 11*	*LAT 12*
Gain Factor	37.96	37.96	37.97	37.94	37.93	37.95	37.92	37.92	37.97	37.94	37.95	38.03
Std. deviation	0.23	0.31	0.30	0.36	0.27	0.31	0.28	0.31	0.30	0.29	0.31	0.36

5. SIS PERFORMACE ACHIEVED

Table 5 and Table 6 show the optical performance of each optical sensor from SIS'20-Field Model instrument. There are situations when the unit is working under normal irradiance conditions as well as under diffuse light. The summary considers two different thermal situations, cold (27 000 "counts") in the Table 5 and warm (53 000 "counts") in the Table 6, to evaluate the noise level in darkness conditions, expressed in [W/m^2], the dynamic range divided between the lower level given by the 10% accuracy and the upper level given by the saturation value, the accuracy and the precision are referring to a coverage of 95%.

Table 5. Optical channel performance for the FM SIS'20 of ExoMars 2020 evaluated in cold conditions for both gain modes, nominal and high configurations.

		Dynamic Range					***Accuracy*** Note 2		***Precision*** Note 3		***Noise*** Note 1	
		[W/m^2]					***[%]***		**[W/m^2]**		***[W/m^2]***	
	Light incident condition	**Lower limit**		**Best RIFOV for changin of gain**	**Upper limit**		***Combined / Relative wiht a coverage of 95 %***					
		HIGH gain	***LOW Gain***	***[Accuracy of both gains are the same]***	***HIGH gain***	***LOW gain***	***High gain***	***Low gain***	***HIGH gain***	***LOW gain***	***HIGH gain***	***LOW gain***
		[Accuracy better than 10%]			***[Saturation]***							
TOP 1	@ Normal incidence	9.12E-02	1.21	3.90	40.05	1530.50	6.18	5.63	4.61E-03	2.14E-02	4.61E-03	2.11E-02
	Under diffuse light	0.12	1.65	5.32	54.60	2086.57	6.18	5.63	6.29E-03	2.91E-02	6.29E-03	2.87E-02
TOP 2	*@ Normal incidence*	5.33E-04	1.05E-02	6.67E-02	0.21	8.12	4.74	4.53	2.20E-05	1.19E-04	2.20E-05	1.19E-04
	Under diffuse light	1.24E-03	2.44E-02	0.16	0.50	18.91	4.72	4.51	5.11E-05	2.77E-04	5.11E-05	2.77E-04
TOP 3	@ Normal incidence	3.37E-03	0.15	0.69	1.94	73.70	6.88	6.68	2.19E-04	4.68E-04	2.19E-04	4.62E-04
	Under diffuse light	7.72E-03	0.35	1.59	4.44	169.23	6.87	6.67	5.03E-04	1.07E-03	5.03E-04	1.06E-03
TOP 4	*@ Normal incidence*	-	-	3.36E-03	7.19E-03	0.27	12.10	12.04	6.68E-06	8.60E-06	6.68E-06	8.59E-06
	Under diffuse light	-	-	7.28E-03	1.56E-02	0.58	12.06	12.01	1.45E-05	1.86E-05	1.45E-05	1.86E-05
TOP 5	@ Normal incidence	1.72E-04	1.08E-03	7.76E-03	1.72E-02	0.65	5.71	5.60	9.99E-06	1.79E-05	9.99E-06	1.78E-05
	Under diffuse light	3.76E-04	2.36E-03	1.71E-02	3.79E-02	1.43	5.63	5.51	2.20E-05	3.93E-05	2.20E-05	3.91E-05
LAT 1	*@ Normal incidence*	6.99E-05	1.28E-03	1.67E-02	1.75E-02	0.66	6.00	5.97	5.13E-06	5.81E-06	5.13E-06	5.77E-06
	Under diffuse light	1.27E-04	2.33E-03	3.41E-02	3.58E-02	1.35	4.48	4.43	1.05E-05	1.19E-05	1.05E-05	1.18E-05
LAT 2	@ Normal incidence	9.91E-04	1.03E-02	7.97E-02	0.13	4.99	7.81	7.77	4.89E-05	7.20E-05	4.89E-05	7.13E-05
	Under diffuse light	1.86E-03	1.93E-02	0.18	0.29	11.12	6.71	6.66	1.09E-04	1.61E-04	1.09E-04	1.59E-04
LAT 3	*@ Normal incidence*	9.32E-05	1.92E-03	1.96E-02	2.29E-02	0.86	6.08	6.03	9.77E-06	8.95E-06	9.77E-06	8.89E-06
	Under diffuse light	1.82E-04	3.78E-03	4.33E-02	5.05E-02	1.91	4.58	4.51	2.16E-05	1.97E-05	2.16E-05	1.96E-05
LAT 4	@ Normal incidence	1.14E-03	1.64E-02	0.11	0.17	6.57	7.83	7.77	4.20E-05	1.20E-04	4.20E-05	1.19E-04
	Under diffuse light	2.03E-03	2.94E-02	0.23	0.37	13.96	6.73	6.66	8.93E-05	2.55E-04	8.93E-05	2.53E-04
LAT 5	@ Normal incidence	8.32E-05	7.46E-04	8.25E-03	1.77E-02	0.67	6.07	6.03	6.16E-06	7.17E-06	6.16E-06	7.11E-06
	Under diffuse light	1.55E-04	1.39E-03	1.71E-02	3.68E-02	1.39	4.57	4.51	1.28E-05	1.49E-05	1.28E-05	1.48E-05
LAT 6	@ Normal incidence	1.10E-03	8.64E-03	6.63E-02	0.17	6.41	7.81	7.77	6.90E-05	5.81E-05	6.90E-05	5.59E-05
	Under diffuse light	1.97E-03	1.55E-02	0.14	0.36	13.61	6.71	6.66	1.46E-04	1.23E-04	1.46E-04	1.19E-04

LAT 7	@ Normal incidence	1.23E-04	7.59E-04	8.27E-03	2.03E-02	0.77	6.07	6.03	5.11E-06	9.76E-06	5.11E-06	9.74E-06
	Under diffuse light	2.25E-04	1.38E-03	1.68E-02	4.14E-02	1.56	4.57	4.51	1.04E-05	1.99E-05	1.04E-05	1.98E-05
LAT 8	@ Normal incidence	8.40E-04	1.22E-02	9.45E-02	0.14	5.40	7.81	7.77	3.18E-05	6.84E-05	3.18E-05	6.77E-05
	Under diffuse light	1.52E-03	2.22E-02	0.20	0.31	11.58	6.71	6.66	6.84E-05	1.47E-04	6.84E-05	1.45E-04
LAT 9	@ Normal incidence	1.32E-03	1.33E-02	0.11	0.20	7.43	7.81	7.77	1.25E-04	9.20E-05	1.25E-04	9.06E-05
	Under diffuse light	2.38E-03	2.41E-02	0.23	0.42	15.86	6.71	6.66	2.66E-04	1.96E-04	2.66E-04	1.94E-04
LAT 10	@ Normal incidence	1.37E-04	1.67E-03	1.74E-02	2.21E-02	0.83	6.08	6.03	1.26E-05	5.01E-06	1.26E-05	4.93E-06
	Under diffuse light	2.55E-04	3.11E-03	3.62E-02	4.61E-02	1.73	4.57	4.51	2.63E-05	1.05E-05	2.63E-05	1.03E-05
LAT 11	@ Normal incidence	6.90E-04	8.17E-03	6.23E-02	0.13	4.86	7.81	7.77	5.46E-05	9.53E-05	5.46E-05	9.48E-05
	Under diffuse light	1.23E-03	1.47E-02	0.13	0.27	10.36	6.71	6.66	1.16E-04	2.03E-04	1.16E-04	2.02E-04
LAT 12	@ Normal incidence	7.25E-05	7.90E-04	6.69E-03	1.61E-02	0.61	6.10	6.03	5.90E-06	8.13E-06	5.90E-06	8.10E-06
	Under diffuse light	1.48E-04	1.62E-03	1.53E-02	3.69E-02	1.40	4.61	4.51	1.35E-05	1.86E-05	1.35E-05	1.85E-05

Table 6. Optical channel performance for the FM SIS'20 of ExoMars 2020 evaluated in cold conditions for both gain modes, nominal and high configurations.

		Dynamic Range					***Accuracy*** Note 2		***Precision*** Note 3		***Noise*** Note 1	
		[W/m²]					***[%]***		**[W/m²]**		***[W/m²]***	
	Light incident condition	**Lower limit**		**Best RIFOV for changin of gain**	**Upper limit**		***Combined / Relative wiht a coverage of 95 %***					
		HIGH gain	***LOW Gain***	***[Accuracy of both gains are the same]***	***HIGH gain***	***LOW gain***	***High gain***	***Low gain***	***HIGH gain***	***LOW gain***	***HIGH gain***	***LOW gain***
		[Accuracy better than 10%]			***[Saturation]***							
TOP 1	@ Normal incidence	7.96E-02	0.33	1.04	36.88	1409.54	6.18	5.63	4.25E-03	1.99E-02	4.25E-03	1.94E-02
	Under diffuse light	0.11	0.44	1.42	50.28	1921.67	6.18	5.63	5.79E-03	2.71E-02	5.79E-03	2.65E-02
TOP 2	*@ Normal incidence*	5.57E-04	1.92E-03	1.19E-02	0.22	8.23	4.74	4.53	2.22E-05	1.21E-04	2.22E-05	1.20E-04
	Under diffuse light	1.30E-03	4.47E-03	0.03	0.50	19.15	4.72	4.51	5.18E-05	2.81E-04	5.18E-05	2.80E-04
TOP 3	@ Normal incidence	6.00E-03	0.02	0.08	1.97	74.86	6.88	6.68	2.22E-04	4.70E-04	2.22E-04	4.70E-04
	Under diffuse light	1.38E-02	0.04	0.19	4.51	171.90	6.87	6.67	5.10E-04	1.08E-03	5.10E-04	1.08E-03
TOP 4	*@ Normal incidence*	4.04E-02	7.65E+03	7.02E-03	5.47E-03	0.27	12.10	12.04	6.98E-06	8.82E-06	6.70E-06	8.61E-06
	Under diffuse light	8.62E-02	1.63E+04	1.52E-02	1.18E02	0.58	12.06	12.01	1.51E-05	1.91E-05	1.45E-05	1.86E-05
TOP 5	@ Normal incidence	6.46E-04	1.01E-03	6.86E-03	1.74E-02	0.70	5.71	5.60	1.08E-05	1.92E-05	1.07E-05	1.91E-05
	Under diffuse light	1.41E-03	2.20E-03	1.51E-02	3.83E-02	1.53	5.63	5.51	2.37E-05	4.22E-05	2.36E-05	4.20E-05
LAT 1	*@ Normal incidence*	1.34E-04	8.07E-04	9.65E-03	1.81E-02	0.69	6.00	5.97	5.33E-06	6.07E-06	5.33E-06	5.99E-06

	Under diffuse light	2.45E-04	1.48E-03	1.97E-02	3.70E-02	1.41	4.48	4.43	1.09E-05	1.24E-05	1.09E-05	1.22E-05
LAT 2	@ Normal incidence	1.34E-03	7.15E-03	5.09E-02	0.14	5.24	7.81	7.77	5.14E-05	7.51E-05	5.14E-05	7.49E-05
	Under diffuse light	2.51E-03	1.35E-02	0.11	0.31	11.68	6.71	6.66	1.15E-04	1.67E-04	1.15E-04	1.67E-04
LAT 3	*@ Normal incidence*	2.37E-04	1.07E-03	1.04E-02	2.37E-02	0.90	6.08	6.03	1.02E-05	9.33E-06	1.02E-05	9.24E-06
	Under diffuse light	4.67E-04	2.12E-03	2.29E-02	5.23E-02	1.98	4.58	4.51	2.24E-05	2.06E-05	2.24E-05	2.04E-05
LAT 4	@ Normal incidence	1.92E-03	1.10E-02	0.07	0.18	6.90	7.83	7.77	4.42E-05	1.25E-04	4.42E-05	1.25E-04
	Under diffuse light	3.43E-03	1.97E-02	0.15	0.39	14.66	6.73	6.66	9.38E-05	2.66E-04	9.38E-05	2.66E-04
LAT 5	@ Normal incidence	1.41E-04	7.65E-04	7.86E-03	1.84E-02	0.70	6.07	6.03	6.41E-06	7.44E-06	6.41E-06	7.40E-06
	Under diffuse light	2.62E-04	1.42E-03	1.63E-02	3.81E-02	1.44	4.57	4.51	1.33E-05	1.54E-05	1.33E-05	1.54E-05
LAT 6	@ Normal incidence	2.23E-03	6.76E-03	4.74E-02	0.18	6.80	7.81	7.77	7.31E-05	6.00E-05	7.31E-05	5.93E-05
	Under diffuse light	3.98E-03	1.21E-02	0.10	0.38	14.43	6.71	6.66	1.55E-04	1.27E-04	1.55E-04	1.26E-04
LAT 7	@ Normal incidence	1.48E-04	8.20E-04	8.45E-03	2.10E-02	0.79	6.07	6.03	5.30E-06	1.02E-05	5.30E-06	1.01E-05
	Under diffuse light	2.69E-04	1.49E-03	1.72E-02	4.27E-02	1.62	4.57	4.51	1.08E-05	2.08E-05	1.08E-05	2.06E-05
LAT 8	@ Normal incidence	1.43E-03	7.81E-03	5.55E-02	0.15	5.61	7.81	7.77	3.31E-05	7.06E-05	3.31E-05	7.05E-05
	Under diffuse light	2.59E-03	1.42E-02	0.12	0.32	12.05	6.71	6.66	7.11E-05	1.52E-04	7.11E-05	1.51E-04
LAT 9	@ Normal incidence	2.77E-03	1.20E-02	0.09	0.21	7.80	7.81	7.77	1.31E-04	9.55E-05	1.31E-04	9.52E-05
	Under diffuse light	4.98E-03	2.16E-02	0.19	0.44	16.66	6.71	6.66	2.80E-04	2.04E-04	2.80E-04	2.03E-04
LAT 10	@ Normal incidence	2.54E-04	9.65E-04	9.49E-03	2.28E-02	0.86	6.08	6.03	1.31E-05	5.27E-06	1.31E-05	5.13E-06
	Under diffuse light	4.74E-04	1.80E-03	1.98E-02	4.75E-02	1.80	4.57	4.51	2.73E-05	1.10E-05	2.73E-05	1.07E-05
LAT 11	@ Normal incidence	1.50E-03	5.82E-03	4.08E-02	0.13	5.10	7.81	7.77	5.74E-05	9.97E-05	5.74E-05	9.96E-05
	Under diffuse light	2.69E-03	1.05E-02	0.09	0.29	10.88	6.71	6.66	1.22E-04	2.13E-04	1.22E-04	2.12E-04
LAT 12	@ Normal incidence	1.61E-04	5.80E-04	4.72E-03	1.67E-02	0.64	6.10	6.03	6.13E-06	8.47E-06	6.13E-06	8.42E-06
	Under diffuse light	3.28E-04	1.19E-03	1.08E-02	3.82E-02	1.45	4.61	4.51	1.40E-05	1.94E-05	1.40E-05	1.93E-05

6. CONCLUSION

The Solar_Irradiance_Sensor (SIS'22) of METEO, the meteorological stations for the Exomars 2022 Kazachok lander has been calibrated and it has achieved the scientific requirements.

The procedure used to calibrate the DREAM-SIS of Schiaparelli lander in ExoMars '16 [11] has been taken as base for this calibration with some improvements:

- correction term added to the calibration offset. The use of this factor produces improvements in the offset determination that are generally insignificant but have reached 2 % in someexceptionalsituations.
- Complete different ARF analysis by using a mathematical model based on the geometry of the FoV mask and additional correction terms to include the effects of wall reflectivity. This allows to characterize the blocking zones that have not been studied so far.
- Calculation and introduction of the spectral correction in the determination of the responsivity. This correction has been lower than 1% in most of the cases and only some of them reached 7%. Nevertheless, the overall effect has not exceeded 2 % in any of the cases.

These improvements will be adopted in the future for the calibration of new radiometers. Deeper research will be needed in the calibration of the ARF and its blocking zone, as in flight results whit RDS are proving that in certain atmospheric conditions it needs a better determination. This will certainly mean looking for more powerful lamps, because the reduction of signal in this FoV area is less than 10e-4, which is the limit imposed on the confidence level of the analysis, determined by the noise and the low light signal that arrives in these conditions.

REFERENCES

[1] Guerrero, H.: Development of miniaturized instrumentation for Planetary Exploration and its application to the Mars MetNet Precursor Mission. In: EGU General Assembly Conference Abstracts 2010,Vol. 12 p. 13330

[2] Apéstigue,V., et al.: DREAMS-SIS: A Miniature Instrument for the Measurement of Atmospheric Optical Depth on ExoMars 2016 EDM. International Workshop on Instrumentation for Planetary Missions – IPM-2014. Greenblet. Maryland (2014)

[3] Esposito, F., Debei, S., Bettanini, C., Molfese, C., Arruego Rodriguez, I., Colombatti, G., Harri, A.M., Montmessin, F., Wilson, C., Aboudan, A., others: The DREAMS Experiment of the ExoMars 2016 Mission for the study of Martian environment during the dust storm Season. In: Eighth International Conference on Mars 2014, p. 1246

[4] Arruego, I., Apéstigue, V., Jiménez, J.J., Martínez-Oter, J., Álvarez-Ríos, F.J., González-Guerrero, M., Rivas, J., Azcue, J., Martín, n., I., Toledo, D., others: DREAMS-SIS: The Solar Irradiance Sensor on-board the ExoMars 2016 lander. Advances in Space Research **60**(1), 103-120 (2017).

[5] Toledo, D., Arruego, I., Apéstigue, V., Jiménez, J.J., Gómez, L., Yela, M., Rannou, P., Pommereau, J.-P.: Measurement of dust optical depth using the solar irradiance sensor (SIS) onboard the ExoMars 2016 EDM. Planetary and Space Science **138**, 33-43 (2017)

[6] http://mars.nasa.gov/mars2020/mission/rover/ Accessed August 2022

[7] Ápestigue,V., Gonzalo,A., Jiménez,J.J., et al. Radiation and Dust Sensor for Mars Environmental Dynamic Analyzer Onboard M2020Rover. Sensors2022,22(8),2907;https://doi.org/10.3390/s22082907

[8] http://exploration.esa.int/mars/48088-mission-overview/ Accessed August 2022

[9] Rodriguez-Manfredi, J. A., et al. (2021). The Mars Environmental Dynamics Analyzer, MEDA. A suite of environmental sensors for the Mars 2020 mission. Space science reviews, 217(3), 1-86.

[10] Newman, C.E. et al. The dynamic atmospheric and aeolian environment of Jezero crater, Mars, Science Advances (in press).

[11] Jiménez,J.J., J Álvarez,F., Gonzalez-Guerrero,M. et al. Calibration OGSEs for multichannel radiometers for Mars atmosphere studies. CEAS Space J10,127–145(2018).https://doi.org/10.1007/s12567-018-0194-8

[12] Wyatt, C.L.: Radiometric Calibration: Theory and Methods, New York: Academic Press, Inc.,(1978).

[13] Wyatt, C.L.: Electro-optical system design for information processing. McGraw-Hill, (1991)

[14] Hülsen, G., Gröbner, J., Bais, A., Blumthaler, M., Disterhoft, P., Johnsen, B., Lantz, K.O., Meleti, C., Schreder, J., Vilaplana Guerrero, J.M., others: Intercomparison of erythemal broadband radiometers calibrated by

seven UV calibration facilities in Europe and the USA. Atmospheric Chemistry and Physics 8(16), 4865-4875 (2008).

[15] Piedehierro, A.A., Cancillo, M.L., Serrano, A., Antón, M., Vilaplana, J.M.: Global irradiance calibration of multifilter UV radiometers. Journal of Geophysical Research: Atmospheres 121(1), 427-438 (2016).

[16] Tansock, J., Bancroft, D., Butler, J., Cao, C., Datla, R., Hansen, S., Helder, D., Kacker, R., Latvakoski, H., Mylnczak, M., others: Guidelines for Radiometric Calibration of Electro-Optical Instruments for Remote Sensing. (2015).

[17] Tansock, J.J., Hansen, S., Paskett, K., Shumway, A., Peterson, J., Stauder, J., Gordley, L.L., Wang, Y., Melbert, M., Russell Iii, J.M., others: SABER ground calibration. International Journal of Remote Sensing 24(2), 403-420 (2003).

[18] Datla, R., Shao, X., Cao, C., Wu, X.: Comparison of the Calibration Algorithms and SI Traceability of MODIS, VIIRS, GOES, and GOES-R ABI Sensors. Remote Sensing 8(2), 126 (2016).